



## Research paper

# The fundamental role and mechanism of reduced graphene oxide in rGO/Pt-TiO<sub>2</sub> nanocomposite for high-performance photocatalytic water splitting

Pengfei Wang<sup>a</sup>, Sihui Zhan<sup>a,\*</sup>, Yuguo Xia<sup>b</sup>, Shuanglong Ma<sup>a</sup>, Qixing Zhou<sup>a</sup>, Yi Li<sup>c</sup><sup>a</sup> College of Environmental Science and Engineering, Nankai University, Tianjin 300350, PR China<sup>b</sup> School of Chemistry & Chemical Engineering, National Engineering Research Center for Colloidal Materials, Shandong University, Jinan 250100, PR China<sup>c</sup> Department of Chemistry, Tianjin University, Tianjin 300072, PR China

## ARTICLE INFO

## Article history:

Received 21 November 2016

Received in revised form 20 January 2017

Accepted 8 February 2017

Available online 13 February 2017

## Keywords:

Reduced graphene oxides

Photocatalysis

Hydrogen generation

DFT calculation

Mechanism

## ABSTRACT

Recently, developing high-efficiency photocatalytic hydrogen generation photocatalysts and clarifying the inherent mechanism behind the enhancement of hydrogen generation activity have been the research focus. Here, we present a step-wise strategy to prepare Pt/TiO<sub>2</sub>/reduced graphene oxide photocatalysts and the inherent mechanism of the enhanced photocatalytic activities were systematically investigated. Experimentally, the 2 wt% rGO doped rGO/Pt-TiO<sub>2</sub> nanocomposites showed the superior solar-driven hydrogen generation rate (1075.68 μmol h<sup>-1</sup> g<sup>-1</sup>), which was 81 times and 5 times higher than bare TiO<sub>2</sub> and Pt/TiO<sub>2</sub> samples, respectively. X-ray photoelectron spectroscopy (XPS) and Fourier transform infrared spectra (FT-IR) demonstrated the formation of Ti—O—C bonds in the hybrid, which drove the shifting upwards of the valence band edge from +2.2 eV to +1.83 eV. Furthermore, photoelectrochemical tests indicated the electron density of PTG-2 was about one order of magnitude higher than TiO<sub>2</sub>. Moreover, DFT calculations displayed that the bandgap had been successfully narrowed from 2.88 eV to 2.76 eV and the original blank energy region located at TiO<sub>2</sub> bandgap was filled with C2p orbitals, which resulted in excited electrons in TiO<sub>2</sub> efficiently transferring to graphene. Consequently, the DFT calculations are in good agreement with the experimental results and physical characterizations. This study affords us a rational design of a high efficiency photocatalytic system for solar energy conversion.

© 2017 Elsevier B.V. All rights reserved.

## 1. Introduction

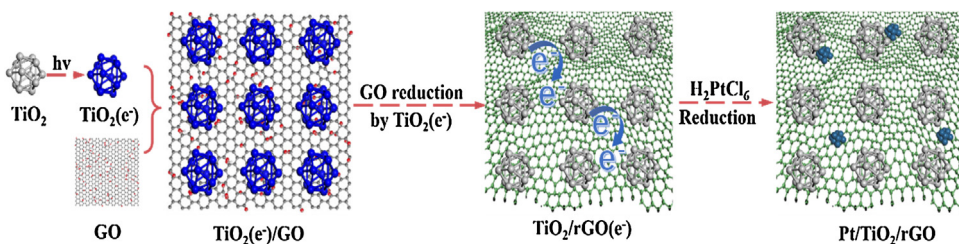
With increasing anxious about the problems of environmental pollution and energy crisis, the hydrogen generation via photocatalytic water splitting as a sustainable strategy for solar energy conversion, is receiving extensive attention, because photocatalytic hydrogen generation, as a secular substitution to replace fossil fuels, provides clean and high-performance energy sources [1,2]. Various semiconductor photocatalysts have been applied to photocatalytic hydrogen generation till now. As efficient photocatalysts in water splitting, the semiconductors must meet several crucial requirements related to appropriate band gap (1.6–2.2 eV), efficient visible light absorption, high carrier mobility, correct band-edge positions that straddle the water redox potentials, and long-term stability against the photo-corrosion in water [3]. Among the vari-

ous semiconductors, TiO<sub>2</sub>, as the earliest and most successful water splitting semiconductor [4], gets most attention in comparison to other semiconductors, because it has many beneficial properties such as chemical inertness, photostability, environmental friendliness, low cost and excellent photocatalytic performance [5,6]. Nevertheless, its optical absorption has been limited to the ultraviolet (UV) region of the solar spectrum because of its large band gap [7]. In addition to its large bandgap, its photocatalytic efficiency also be hampered by the rapid recombination of photo-generated carriers [8].

Over the past decade, a lot of efforts have been made to narrow the bandgap of TiO<sub>2</sub> by various of effective strategies including self-doping, doping with other elements or coupling with low bandgap semiconductors [9], so as to extend its light absorption to visible light region and increase its visible light conversion. Generally, although the band gap can be effectively narrowed by the efforts, they also take some negative effects to other important criteria. For instance, inorganic elements have been widely doped with TiO<sub>2</sub> to reduce the band gap, and the high concentration of impurities are

\* Corresponding author.

E-mail address: [sihuizhan@nankai.edu.cn](mailto:sihuizhan@nankai.edu.cn) (S. Zhan).



**Scheme 1.** Schematic preparation procedure of PTG nanocomposite.

needed in most cases. However, these impurities often give rise to serious photoinduced electron-hole pairs recombination, which significantly reduce photocatalytic hydrogen generation efficiency [10].

Actually, the more efficient strategy to enhance the photocatalytic hydrogen generation efficiency of  $\text{TiO}_2$  is to restrain the photoinduced electron-hole pair recombination [11]. It is reported that the carriers recombination rate constant in bulk  $\text{TiO}_2$  is about  $5 \times 10^{-13} \text{ cm}^{-3} \text{ s}^{-1}$ , which is about 3 orders of magnitude faster than its migration rate constant [12]. As a result, only about 10% of the carriers involve in the photocatalytic reaction. And various of techniques have been pursued to suppress the rapid recombination of the carriers, such as downsizing the photocatalysts to accelerate the migration of carriers [13], improving the crystallinity to decrease the defect densities [14], constructing heterojunctions [15], and loading co-catalysts [16,17].

Recently, combining  $\text{TiO}_2$  with carbon materials [e.g., fullerenes ( $\text{C}_{60}$ ), carbon nanotubes (CNT) and graphene] has been regarded as an important method for enhancing the photocatalytic activity of  $\text{TiO}_2$  [18]. And among various of carbon materials, graphene, a two-dimensional (2D) network of hexagonal structured  $\text{sp}^2$ -hybridized carbon atoms, has attracting great research interests in various energy conversion applications. The excellent properties of graphene indicated that it has enormous potential to be an ideal construction component of photocatalytic materials for hydrogen generation [19]. The previous studies show that photo-generated electrons can migrate from the conduct bands of semiconductors to graphene, which can efficiently suppress the recombination of photoinduced carriers and promote photocatalytic hydrogen generation [20]. In addition, the extremely high conductivity of graphene can make the accepted electrons migrate rapidly across its 2D plane to active sites for hydrogen generation [21]. Thus, the role of graphene as an electron acceptor and transporter has been classified by various photocatalytic experiments. Nevertheless, many challenges on the graphene-based materials for hydrogen generation are still needed to be overcome. Especially, the inherent mechanism behind the enhancement of hydrogen generation activity is needed to be clarified, and theoretical calculation is a powerful technology to simulate the specific microstructures and provide in-depth insight to the electronic properties of nanomaterials, giving us a better understanding of the experimental phenomena [19]. Importantly, to our knowledge, the mechanism of reduced graphene oxide with doubly nanoparticles in photocatalytic hydrogen generation has not been clearly studied so far.

Herein we present a stepwise synthesis method for the preparation of hybrid nanomaterial based on  $\text{Pt}/\text{TiO}_2/\text{rGO}$  as a model system for photocatalytic hydrogen generation and the inherent mechanism of the enhanced photocatalytic activities were systematically investigated. Experimentally, an efficient super-high solar-driven hydrogen production rate of  $1075.68 \mu\text{mol h}^{-1} \text{ g}^{-1}$  is obtained, which is much greater than the pristine  $\text{TiO}_2$ . X-ray photoelectron spectroscopy (XPS) and Fourier transform infrared spectra (FT-IR) demonstrated the formation of  $\text{Ti}-\text{O}-\text{C}$  bonds in the hybrid, which drove the shifting upwards of the valence band edge.

The extensive sophisticated density-functional theory (DFT) calculations display that the bandgap has been successfully narrowed and the interfacial charge transfer property has been remarkably strengthened.

## 2. Experimental

### 2.1. Synthesis of PTG samples

The GO, which was obtained from the oxidation of graphite powder using the well-known modified Hummers method [22], can be easily dispersed in polar solvents. In order to combine  $\text{TiO}_2$  and Pt nanoparticles with rGO, we developed a stepwise process. Firstly, 0.5 g  $\text{TiO}_2$  was dispersed in 80 mL ethanol. Then the solution was irradiated by a 300 W Xenon lamp equipped with AM 1.5G filter under continuous magnetic stirring, thus the electrons were excited and stored in  $\text{TiO}_2$  nanoparticles. Secondly, a certain volume of GO suspension in ethanol was added gradually to the  $\text{TiO}_2$  suspension to introduce GO reduction and store excess electrons. Thirdly, 3.4 mL  $\text{H}_2\text{PtCl}_6$  (0.0077 M) was added and the platinum ions were reduced by the stored electrons in rGO, causing deposition of Pt nanoparticles on rGO. Finally, the sample was dried at 80°C in vacuum overnight to obtain  $\text{Pt}/\text{TiO}_2/\text{rGO-x}$  (PTG-x) containing 1.0 wt% Pt and x (0.5, 1, 1.5, 2, 3, 5) wt% rGO (Scheme 1). For comparison,  $\text{Pt}/\text{TiO}_2$  (PT) and  $\text{TiO}_2/\text{rGO}$  (TG-x) samples were prepared using the same method without the addition of GO or  $\text{H}_2\text{PtCl}_6$ .

### 2.2. Material characterizations

Power X-ray diffraction (XRD) patterns were obtained on an X-ray diffractometer (Rigaku D/Max 2200PC, Japan) using  $\text{Cu K}\alpha$  radiation ( $\lambda = 0.15418 \text{ nm}$ ) with 40 kV accelerating voltage and 40 mA applied current over a  $2\theta$  range between 10° and 80° at a scan rate of  $8^\circ \text{ min}^{-1}$ . The morphology and inner structure of the prepared samples were detected by the field-emission scanning electron microscope (FESEM, JSM-6700F at an accelerating voltage of 3 kV, Japan) and transmission electron microscopy (TEM, a JEOL JEM-2100F at an accelerating voltage of 200 kV, Japan). The high-angle annular dark-field scanning transmission electron microscopy (HAADF-STEM) characterization was performed on a JEOL JEM-ARF200F TEM/STEM with a spherical aberration corrector. The specific surface areas were measured by Brunauer-Emmett-Teller (BET) method, the pore size distributions of the samples were recorded by the adsorption branches and a cylindrical pore model (BJH method) with a ASAP 2460 surface area and porosity analyzer at liquid nitrogen temperature. X-ray photoelectron spectroscopy (XPS) data were obtained with a Thermal ESCALAB 250 electron spectrometer using  $\text{Al K}\alpha$  radiation X-ray source ( $h\nu = 1486.6 \text{ eV}$ ). The Fourier transform infrared spectra (FTIR) of the samples were recorded using a Thermo Nicolet iS5 FTIR spectrometer equipped with a liquid-nitrogen-cooled MCT detector. Measurements of Raman spectra were performed on a Bruker RFS 100/S Raman microscope with excitation laser beam wavelength of

1064 nm. The UV-vis diffuse reflection spectra (DRS) were obtained for the dry-pressed disk samples using a UV-vis spectrophotometer (Shimadzu Corporation, UV-3600, Japan) equipped using BaSO<sub>4</sub> as a reflectance standard. The photoluminescence (PL) spectra were measured on an Edinburgh Instruments FLS920P equipped with a Xe lamp-920 at room temperature. Electron spin resonance (ESR) signals of spin-trapped paramagnetic species with 5,5-dimethyl-l-pyrroline N-oxide (DMPO) were carried out on a Bruker model A300 spectrometer. DMPO/H<sub>2</sub>O was prepared by a conventional method. The experimental process was as follows: 0.1 g samples were dispersed in 3 mL deionized water, then 250 μL above-mentioned solution and 200 μL DMPO were dissolved in 5 mL deionized water and stirred for 10 min. And the resulted solution was used as the detection of hydroxyl radicals (DMPO-•OH).

### 2.3. Photocatalytic hydrogen generation test

The photocatalytic experiments were performed in a test installation. The photo reactor is a quartz flask of 150 mL. A full spectrum solar simulator (CEL-S500) with AM 1.5G filter is used as the light source with about 1 Sun power. In a typical photocatalytic experiment, 100 mg of samples were suspended in 100 mL aqueous solution containing 10 vol% triethanolamine (TEOA) as a sacrificial reagent. Then the reaction system was thoroughly degassed by evacuation. Next, the suspensions were illuminated under continuous magnetic stirring. The resultant gas spread into the quantitative loop (1 mL) of a six-way valve, the gas volume was analyzed by gas chromatography (GC2060, Shanghai, China, thermal conductivity detector, 5 Å molecular sieve column and Ar carrier) every 60 min to determine the hydrogen generation rate.

### 2.4. Photocatalytic degradation of methyl orange

The photocatalytic degradation of MO by samples was performed at ambient temperature (25 °C). 50 mg sample was suspended in an aqueous solution (20 mL) containing organic dye of MO (10 mg/L), then the mixture was illuminated under different conditions and stirred continuously. During the degradation process, the sample was taken at different time intervals from the vessel, and subsequently analyzed by UV-vis spectroscopy.

### 2.5. Theoretical calculation

First principal calculations were used to identify the electronic structure changes of P25 after composited with rGO. As shown in HRTEM (Fig. 1), almost all the exposed planes were identified the anatase phase. Therefore, a cluster model consisting of anatase phase TiO<sub>2</sub> and graphene was constructed to simulate their mutual interaction and electronic structure changes. Bulk anatase TiO<sub>2</sub> ( $a=3.776\text{ \AA}$ ,  $c/a=2.512$ , space group: I41/AMD) was firstly relaxed with LDA+U method (Ti( $U^d$ ) = 8 eV, O( $U^p$ ) = 6 eV)[23] which revealed good electronic corrections for antase TiO<sub>2</sub> as shown in Fig. SX. Then, 10 Å dimensional spherical antase TiO<sub>2</sub> cluster consisted of 28 O, 12 Ti atoms was constructed, and 4 H atoms were employed to compensate surface dangling bonds. Besides, two dimensional structure involving 84C atoms was constructed to simulate the rGO substrate. 10 Å vacuum regions were added to eliminate interactions between two images. The adhesion energy was obtained according to the following equation:

$$E_{ad} = E_{com} - E_{graphene} - E_{TiO_2}$$

where  $E_{com}$ ,  $E_{graphene}$  and  $E_{TiO_2}$  represent the total energies of the relaxed graphene-TiO<sub>2</sub> composite, pure graphene and TiO<sub>2</sub> cluster, respectively.

The density functional theory (DFT) calculations were performed using the VASP code [24,25] with the projected augmented wave (PAW) method. Local-density approximation [26] was used for the exchange correlation functional. The valence configurations of the pseudopotentials were  $2s^22p^4$  for O,  $3s^23p^64s^13d^3$  for Ti,  $2s^22p^2$  for C and  $1s^1$  for H. The cutoff energy of the basis function was 400 eV. A Monkhorst-Pack k-point set of  $7 \times 7 \times 3$  was used for the TiO<sub>2</sub> geometry optimization and Γ-point only was used for graphene substrate and hybrid structure. All geometry relaxation was performed until the residual forces on each ion converged to be smaller than 0.02 eV/Å.

### 2.6. Photoelectrochemical measurements

The series of samples (TiO<sub>2</sub>, PT, TG PTG-2) were fabricated into photoanodes as follows: 20 mg sample, 1 mL ethanol and 20 μL nafion were mixed by sonication for 30 min to make a slurry. Then the slurry was dropped onto an indium-tin oxide glass (ITO glass) by a dropper. After the ethanol evaporated thoroughly at ambient temperature, the glasses were dried at 60 °C for 8 h to obtain working electrodes with a similar film thickness. The working electrode areas of the photoanodes are 12 cm<sup>2</sup>. Photoelectrochemical (PEC) performances of the prepared photoanodes were evaluated in a standard three-electrode system (an Ag/AgCl electrode reference electrode and a Pt foil counter electrode) using an electrochemical work station (CHI660D Instruments). 0.5 M NaSO<sub>4</sub> solution was used as the electrolyte. The measured potential vs. Ag/AgCl were converted to reversible hydrogen electrode (RHE) scale via the Nernst equation  $E_{RHE} = E_{Ag/AgCl} + 0.197 + 0.059 \text{ pH}$ . A 300 W Xe lamp was used as a light source. Typically, J-V curves were measured at a scan rate of 5 mV s<sup>-1</sup> and the chopped illumination was used to examine transient photocurrents. Transient photocurrent measurements at a constant bias (0.5 V) with chopped illumination were also conducted to examine the steady-state photocurrent densities of the photoanodes. Electrochemical impedance spectra (EIS) were carried out in the frequency range of 0.0510<sup>5</sup> Hz. Mott-Schottky plots were measured at a frequency of 1 kHz under dark condition.

## 3. Results and discussion

### 3.1. Synthesis and physical characterizations

**Scheme 1** featured the schematic preparation procedure of the stepwise photo-reduction synthesis of PTG nanocomposite. TiO<sub>2</sub> was irradiated in methanol to excite electrons firstly, then the electrons were easily transferred to GO, leading to the reduction of GO into rGO and the recovery of TiO<sub>2</sub>. Finally, the platinum ions were reduced by the stored electrons in rGO, causing deposition of Pt nanoparticles. The crystalline phase of TiO<sub>2</sub>, GO, PT, TG-2 and a series of Pt/TiO<sub>2</sub>/rGO composites denoted as PTG-x (x stands for wt% of rGO in the sample) were analyzed by X-ray diffraction. The XRD patterns of the GO, TiO<sub>2</sub>, PT, PTG-x, and TG-2 samples are shown in Fig. S1. For TiO<sub>2</sub>, obvious crystal planes of anatase and rutile TiO<sub>2</sub> were observed. And the peaks at 2θ value of 25.3°, 37.8°, 48.0°, 54.0°, 62.7°, 68.8°, 70.3° and 75.1° were indexed as (101), (004), (200), (105), (211), (204), (116), (220) and (215) peak observed for anatase TiO<sub>2</sub>. What is more, the peaks at 27.5°, 36.1° and 41.2° were indexed at (110), (101) and (111) crystal planes of rutile TiO<sub>2</sub> [27]. It indicated that the predominant phase of TiO<sub>2</sub> was anatase phase, and it played a leading role in the photocatalytic reaction. For graphene oxide, the peak at 11° was indexed to (001) crystal plane (interlayer spacing of 0.83 nm) and it indicated the complete oxidation graphite to GO [28]. Notably, PT, TG-2 and all PTG-x samples show a similar XRD pattern as TiO<sub>2</sub>. No diffraction

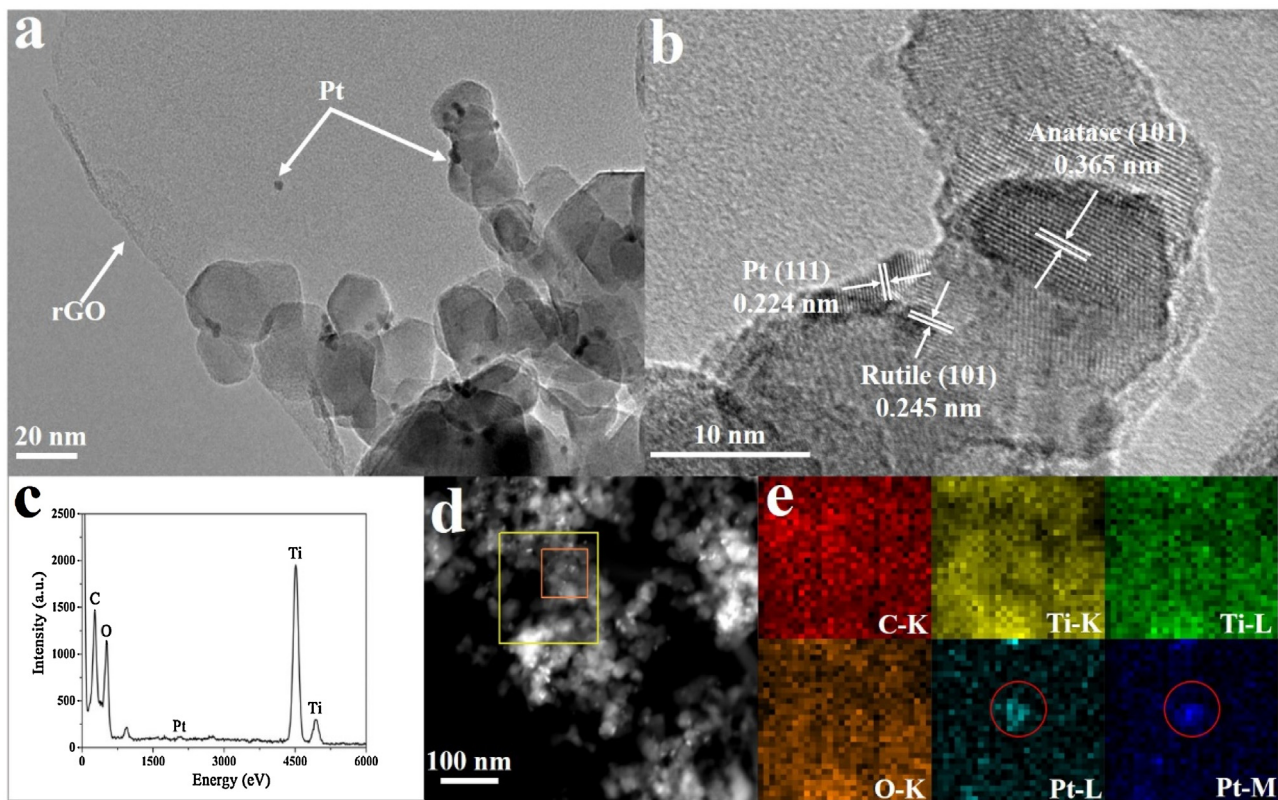


**Fig. 1.** TEM (a), HRTEM (b), EDS (c), HAADF-STEM (d) and elemental mapping (e) of PTG.

peaks for Pt nanoparticles were observed in PT and PTG-x samples, which might be ascribed to the low content and diffraction intensity [29]. In addition, no diffraction peaks for carbon species were observed in TG-2 and PTG-x samples, which can be ascribed to the small amount and weak intensity of rGO, so the peak of rGO at 24.5° might be shielded by the peak of TiO<sub>2</sub> at 25.3° [27,30]. However, the presence of Pt nanoparticles and rGO sheets could be proved by TEM, XPS, FTIR and Raman spectroscopy, which would be discussed later.

Furthermore, the combination mode of Pt, TiO<sub>2</sub> nanoparticles with rGO was characterized by scanning electron microscope (SEM) and transmission electron microscopy (TEM). The morphology of prepared GO was shown in Fig. S2a, b. The prepared GO exhibited thick sheet morphology with ripples, which might provide enough surface area to support Pt and TiO<sub>2</sub> nanoparticles. For PTG sample, energy-dispersive X-ray (EDX) spectrum in Fig. 1c revealed the existence of C, O, Pt and Ti, which exhibited the existence of Pt, TiO<sub>2</sub> and rGO. Furthermore, Pt and TiO<sub>2</sub> nanoparticles were distributed on the surface of rGO sheets (Fig. S2 and Fig. 1a). As can be seen from Fig. 1a, rGO sheets seemed extremely thin, which could increase the surface area and provide good potential for carrier transport [28]. The HRTEM image in Fig. 1b displayed clear lattice fringes of Pt and TiO<sub>2</sub> nanoparticles. The interplanar spacing of 0.224 nm by inverse Fourier transform of the region was the d-spacing value of the Pt (111) plane, corresponding to the face-centered cubic (fcc) lattice with the crystal plane [29]. The fringes of spacing 0.365 and 0.245 nm corresponded to (101) plane of anatase TiO<sub>2</sub> and (101) plane of rutile TiO<sub>2</sub>, respectively. Elemental mapping of C, O, Ti and Pt in PTG sample was given in Fig. 1e, which revealed that Pt and TiO<sub>2</sub> nanoparticles dispersed uniformly on rGO sheets. As a powerful tool for discerning heavy particles, high-angle annular dark-field scanning transmission electron microscopy (HAADF-STEM) was used to confirm the distribution and configuration of Pt on rGO [31,32]. And the HAADF-STEM images in Fig. 1d and Fig. S4 clearly

revealed that Pt nanoparticles were uniformly dispersed on the surface of rGO. Moreover, Pt nanoparticles were either distributed on the surface of rGO in isolation or stuck with TiO<sub>2</sub> on rGO, which could be confirmed by Fig. 1a and Fig. S3. And this revealed that the introduction of rGO could efficiency inhibit the agglomeration of Pt and TiO<sub>2</sub> nanoparticles, which could enhance the utilization efficiency of Pt and the photocatalytic activity.

X-ray photoelectron spectroscopy was used to further conform the interactions among Pt, TiO<sub>2</sub> and GO. The XPS full spectrum of PTG-2 was shown in Fig. 2a. As can be seen from the survey spectrum, there were Pt, C, Ti and O in the composite. And this indicated that the ternary composite had been fabricated successfully. The O 1 s spectrum of PTG-2 was shown in Fig. 2b. The main peaks centered at 529.08, 530.89 and 532.05 eV correspond to Ti—O—Ti (lattice O), Ti—O—C and C—O groups respectively [33]. And the existence of the Ti—O—C bond indicated that rGO had the intense attraction to TiO<sub>2</sub>. The two symmetric peaks at 464.6 and 458.8 eV in PTG-2 for Ti 2p<sub>1/2</sub> and Ti 2p<sub>3/2</sub> spin-orbital splitting photoelectrons in the Ti<sup>4+</sup> chemical state, respectively [34], were slightly shifted towards a higher binding energy compared with those in TiO<sub>2</sub>, which demonstrated that the chemical environment of Ti in PTG-2 had been changed due to the formation of Ti—O—C bond [35]. Fig. 2d showed the C 1 s XPS spectrum of GO. For GO, the bands located at binding energies of 284.6, 287.0, 288.2 and 289.1 eV could be assigned to C—C in aromatic rings, C—O, C=O and COOH groups, respectively, which indicated the complete oxidation graphite to GO [36]. For PTG-2 (Fig. 2e), however, the obvious weaken oxygenated function groups (C—O and COOH) in the composite demonstrated the reduction of GO. This result implied the reduction GO to rGO by photocatalytic reduction. Fig. 2f described the Pt 4f XPS spectrum, and the two peaks could be assigned to the Pt 4f<sub>5/2</sub> and Pt 4f<sub>7/2</sub> [37]. However, the binding energy of Pt 4f<sub>7/2</sub> was 68.4, which was lower than the standard binding energy of Pt metal (71.0 eV) [38], and the platinum in PTG-2 composite should

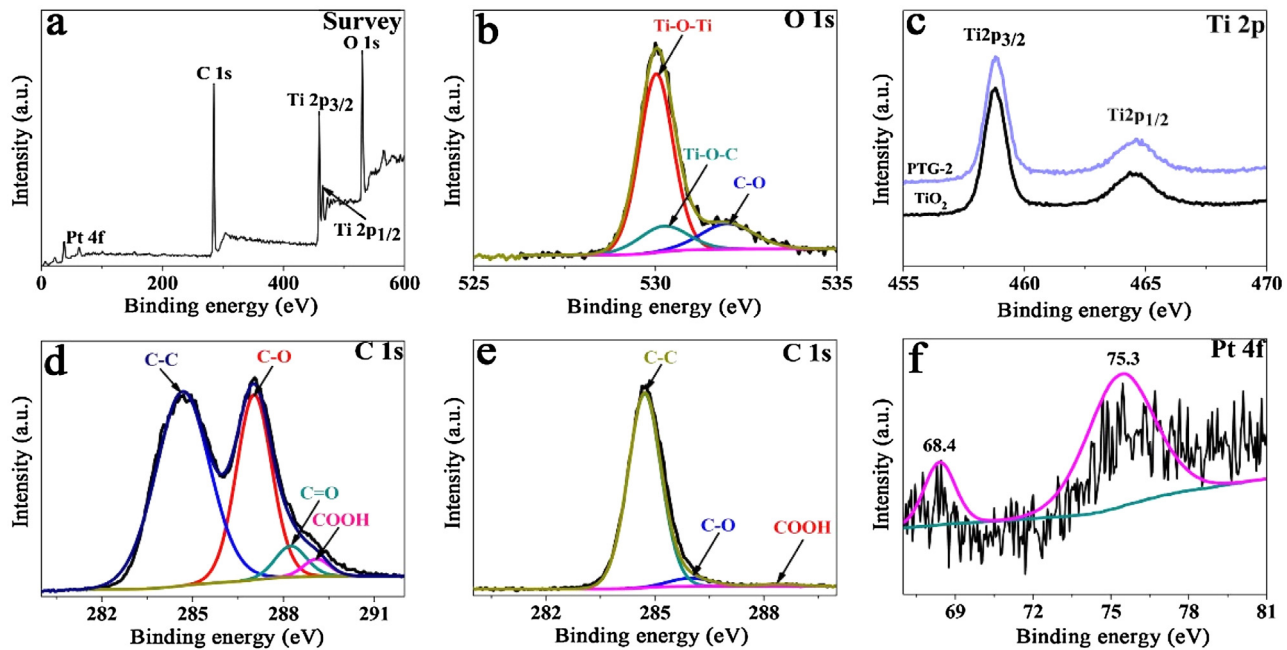


**Fig. 2.** (a) XPS full spectrum for PTG-2. Core level XPS spectra of (b) O 1s, (c) Ti 2p, (d) C 1s, (e) C 1s and (f) Pt 4f for  $\text{TiO}_2$ , PTG-2 and GO.

be considered as a metallic form but in an electron-deficient state [38,39].

Fourier transform infrared (FTIR) spectra of GO and PTG-2 samples were measured to study the different functional groups and chemical bonds, which included  $\text{Ti}-\text{O}-\text{Ti}$  vibrations and  $\text{Ti}-\text{O}-\text{C}$  vibrations. The comparison of the FTIR spectra of GO,  $\text{TiO}_2$  and PTG-2 were shown in Fig. 3a. For  $\text{TiO}_2$ , the spectra showed a broad absorption peak around  $500 \text{ cm}^{-1}$ , which was attributed to the  $\text{Ti}-\text{O}-\text{Ti}$  stretching vibrations. The presence of absorption peak around  $3400 \text{ cm}^{-1}$  was attributed to the O-H stretching frequency, which came from the surface hydroxyl groups. In the case of GO, there were five characteristic peaks in the region of  $1000$ – $3500 \text{ cm}^{-1}$ . The peaks at  $1048$ ,  $1392$ ,  $1628$ ,  $1726$ , and  $3432 \text{ cm}^{-1}$  were attributed to the C-O stretching vibrations, C-O-H groups stretching, O-H bending vibration of epoxide groups and skeletal ring, C=O stretching of COOH groups and O-H stretching [40,41]. For PTG-2, however, the peaks of oxygen functional groups were decreased dramatically in intensity or even disappeared, and the peak at  $1628 \text{ cm}^{-1}$  was attributed to C=C bond, which came from the skeletal vibration of rGO sheets [42]. And the presence of absorption peak below  $1000 \text{ cm}^{-1}$  was attributed to the  $\text{Ti}-\text{O}-\text{Ti}$  and  $\text{Ti}-\text{O}-\text{C}$  stretching vibrations [43]. As a result, the chemically bonded PTG composites were synthesized by the residual carboxylic groups interacted with the surface hydroxyl groups of  $\text{TiO}_2$  during mixing GO with  $\text{TiO}_2$  nanopowder [44].

As a powerful tool for the characterization of carbon-based materials, the Raman spectra were used to further distinguish between  $\text{sp}^2$  and  $\text{sp}^3$  hybridization in carbonaceous materials [45]. Among the two main characteristic Raman bands, G-band was originating from the doubly degenerated zone center  $E_{2g}$  vibrational mode of  $\text{sp}^2$  bonded carbon atoms and D-band was originating from the disorder. Fig. 3b shows the Raman spectra of GO,  $\text{TiO}_2$  and PTG-2 composite. For  $\text{TiO}_2$ , there were four characteristic peaks, and the peaks at  $146$ ,  $397$ ,  $516$  and  $639 \text{ cm}^{-1}$  were attributed to the  $E_g$ ,  $B_{1g}$ ,  $A_{1g}$  and  $E_g$  modes of  $\text{TiO}_2$  anatase phase, respectively [46]. The peaks were also observed in PTG-2 composite, but their intensity decreased significantly. In the case of GO, two typical features of GO were showed in the spectrum, which were D band located at  $1354 \text{ cm}^{-1}$  and G band at  $1587 \text{ cm}^{-1}$  [46]. The D band and G

band corresponded to ring-breathing modes of  $\text{sp}^2$  carbon atoms which were adjacent to a defect or an edge and  $\text{sp}^2$  carbon atoms which were in a planar and conjugated structure [18]. For PTG-2 composite, the D band and G band were slightly red-shifted to  $1353 \text{ cm}^{-1}$  and blue-shifted to  $1594 \text{ cm}^{-1}$  respectively, which was ascribed to a change of surface strain after combination with  $\text{TiO}_2$  [47]. Furthermore, the ratio of D/G band intensity of PTG-2 was 0.806, which was higher than that of GO (0.799), and the increase of the ratio demonstrated a decrease of  $\text{sp}^2$  domain size [18]. And this implies the reduction of GO by photocatalytic reduction led to the formation of new extended  $\text{sp}^2$  domains. As a result, after the photocatalytic reduction process, the GO had been reduced to rGO. So the Raman investigation supported the successful synthesis of PTG composite.

### 3.2. Optical and photocatalytic hydrogen generation properties of the PTG nanocomposites

To gather more insights on the physicochemical properties of the PTG composites, we carefully investigated the optical properties of the samples. Fig. 4a showed the absorbance of  $\text{TiO}_2$  and PTG-x samples, which was measured by UV-vis diffuse reflectance spectroscopy, indicating there were typical semiconductor adsorption-peaks. A comparison of  $\text{TiO}_2$  with PTG-x samples showed that the PTG-x samples not only exhibited a broad background absorption in the visible-light region, but also exhibited a red shift in the absorption edge. This was a very common and widely phenomenon in the doping modifications of semiconductors [48]. The transition energy of photoexcited electrons would be decreased by the combination of  $\text{TiO}_2$  and rGO. Meanwhile, the PTG-x samples showed stronger broad background absorption with increasing rGO content. These results were ascribed to the presence of rGO and the narrowing of the band gap of  $\text{TiO}_2$  [49]. Fig. 4b displayed the photographs of  $\text{TiO}_2$  and PTG-x composites, indicating that the color of PTG-0.5 became grey. And with increased dosage of rGO, the samples became darker and darker, which facilitated the visible absorption of the photocatalysts [50]. Furthermore, to determine the optical band gap ( $E_g$ ), we plotted the Tauc plot [i.e., the curve of converted  $(\alpha h\nu)^l$  versus  $h\nu$ ] from the UV-vis absorption spectrum,

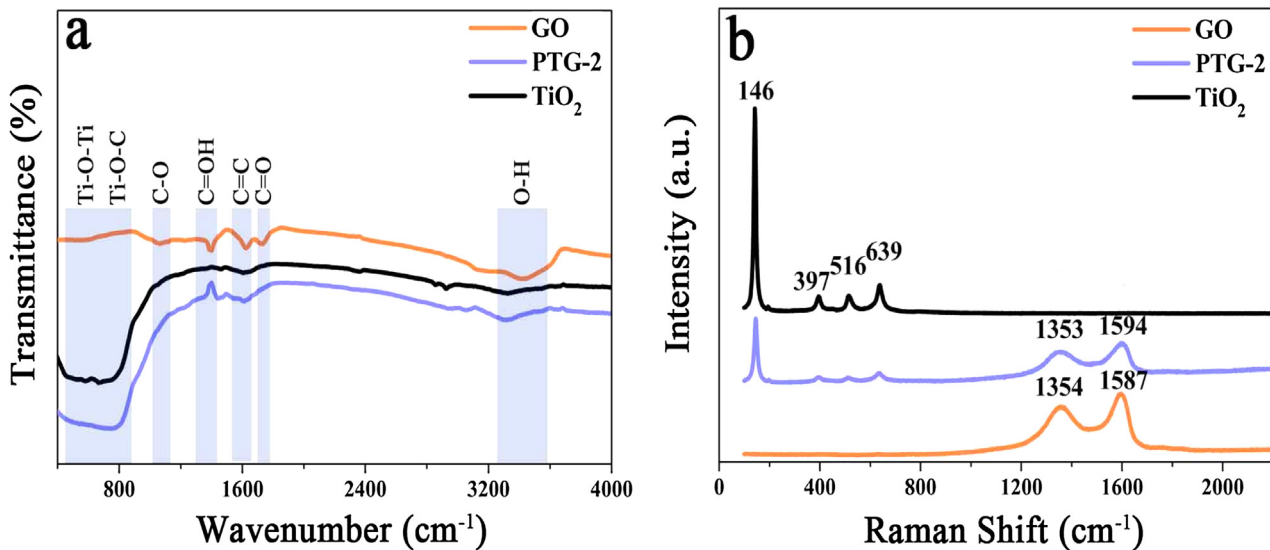


Fig. 3. (a) FTIR spectra and (b) Raman spectra of GO,  $\text{TiO}_2$  and PTG-2.

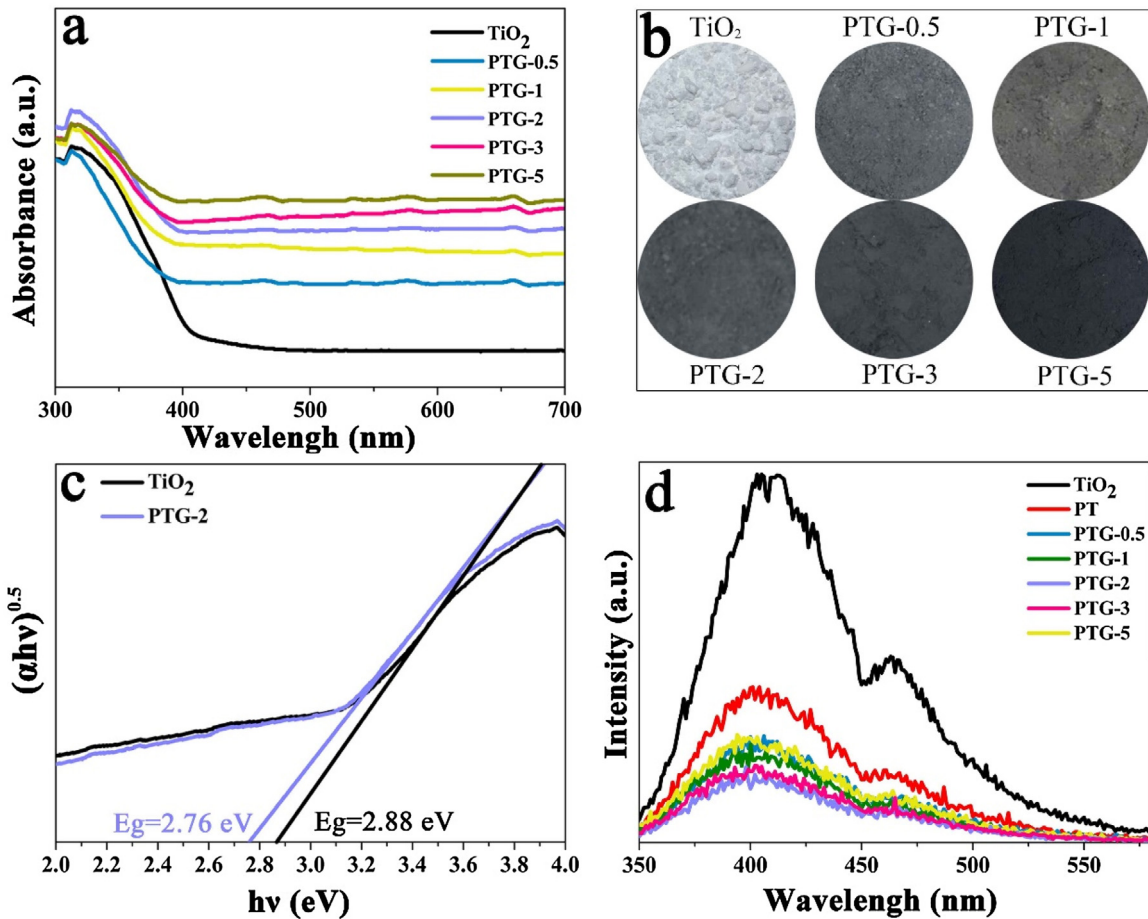
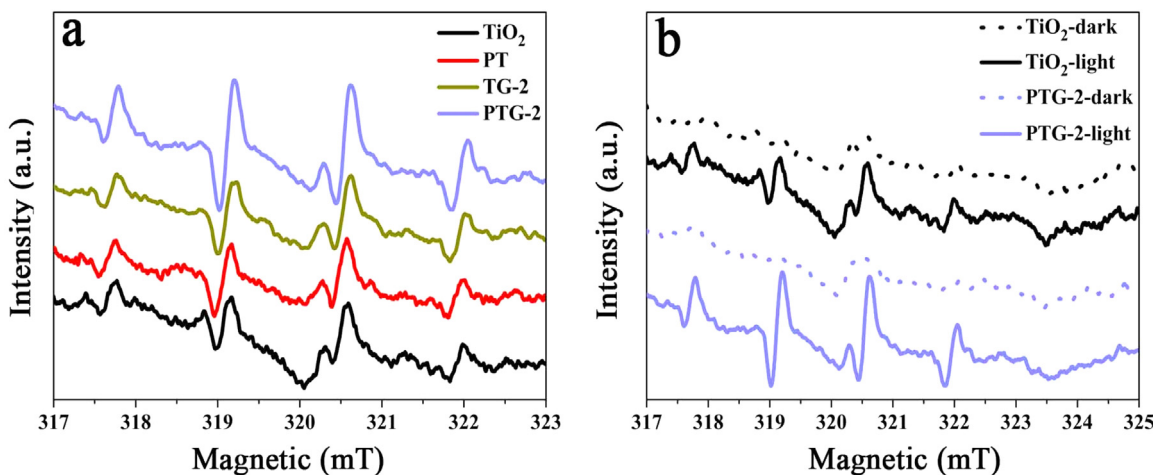


Fig. 4. UV-vis DRS spectra (a), exact appearance (b), bandgap energy (c) and room-temperature PL (d) of  $\text{TiO}_2$ , PT and PTG-x composites.

where  $\alpha$  was the absorption coefficient,  $h$  was Planck constant and  $\nu$  was light frequency, respectively, and  $r=2$  for a direct band gap semiconductor and  $r=1/2$  for an indirect band gap semiconductor [51]. Fig. 4c showed the Tauc plots for  $\text{TiO}_2$  and PTG-2 nanocomposite, and we could see that it showed a good linear fit when using  $r=1/2$ , claiming  $\text{TiO}_2$  to be a direct band gap material (no good lin-

ear fit was obtained for  $r=2$ ). And the  $E_g$  value of PTG-2 was thus determined to be 2.76 eV by measuring the x-axis intercept of an extrapolated line from the linear regime of the plot (Fig. 4c, red plot), while the band gap of  $\text{TiO}_2$  was 2.88 eV. And an apparent tail between 2.0 and 3.2 eV was found in the Tauc plot curve of PTG-2, which could improve the light absorbance and photocatalytic



**Fig. 5.** ESR signals of the DMPO-•OH in aqueous dispersion.

efficiency [52]. The Eg value, as speculated, was less than that of TiO<sub>2</sub>, signifying the effect of the synergistic effect of TiO<sub>2</sub> and the underlying rGO on the TiO<sub>2</sub> domains, caused by the Ti—O—C bonds formation which were confirmed from the XPS and FT-IR spectra. The introduction of rGO into TiO<sub>2</sub> always generated impurity energy levels above the valence band edge, and fewer input energy was involved for the excitation of charge carriers, and thus decreasing the optical absorption band gap [48]. The strong absorption ability could greatly promote the photocatalytic ability of the photocatalysts [29]. As a result of the extended photoresponding range, the PTG-x samples could achieve a more efficient utilization of the spectrum and their photocatalytic ability could be greatly improved in the visible region, which would be proved in the Photocatalytic H<sub>2</sub>-Generation Activity section.

Photoluminescence (PL) quenching effect has been widely used to survey charge transfer effect in semiconductors, and the recombination of electron-hole pairs would give rise to the PL emission signal. So, the PL spectra were carried out to determine the effect of Pt and rGO on the separation of photo-generated electrons and holes. As shown in Fig. 4d, a broad luminescence peak could be observed in the region of 350–550 nm for all samples. And the centered peak at around 400 nm, could be attributed to the band-band PL phenomenon with the energy of light approximately equal to the band-gap energy of TiO<sub>2</sub> [53]. As can be seen, the PL intensity of PT decreased after the deposition of Pt. Furthermore, the PTG-x samples showed much weaker PL intensity than TiO<sub>2</sub> and PT, indicating that the separation ratio of the photogenerated electron-hole pairs had been enhanced. And the remarkable PL quenching was caused by the efficient electron transfer from TiO<sub>2</sub> to Pt through rGO. Besides, PTG-2 composite showed the weakest PL intensity, indicating that there was an optimal value for rGO. And this would efficiently enhance the photocatalytic activity of PTG-2 composite by inhibited the recombination of photoinduced electron-hole pairs, which caused by the electrons transfer from TiO<sub>2</sub> donor to the rGO acceptor quenches the PL with a corresponding increase in the yield of photogenerated mobile charge carriers [54].

More optical and electronic properties of the samples were examined by room temperature electron spin resonance (ESR). The ESR was a powerful technique, which was used to detect radicals in reaction systems. It can be applied to identify the trap population and recombination behavior of the electrons and holes, and the photo-induced radicals via spin-trapping could be directly or indirectly detected, which can be used to identify the electron and hole surface and lattice trapping sites [55]. And DMPO was generally used for trapping radicals, such as DMPO-•OH or DMPO-O<sub>2</sub><sup>•-</sup> [56].

As shown in Fig. 5a, TiO<sub>2</sub>, PT, TG and PTG-2 samples all showed obvious DMPO-•OH signals after irradiation, which revealed the generation of electron-hole pairs. In addition, the signal intensity of PTG-2 was more strengthen than others, which certified that the introduction of rGO can effectively accelerate the electron mobility. Furthermore, greatly enhanced ESR intensities for both TiO<sub>2</sub> and PTG-2 samples were presented under light irradiation (Fig. 5b), indicating the efficient generation of photochemical radical pairs in the PTG nanocomposites. And the strongest signal of PTG-2 sample accounted for the highest photocatalytic performance than other samples.

The photocatalytic hydrogen production on various samples was investigated under the full solar wavelength range of light using triethanolamine (TEOA) as a sacrificial reagent. The continuous hydrogen production profile and the rate of hydrogen production for various samples were shown in Fig. 6a and b, respectively. As can be seen from these curves, the Pt and rGO contents had a significant influence on the photocatalytic activity of TiO<sub>2</sub>. For TiO<sub>2</sub>, it just exhibited very limited H<sub>2</sub> generation efficiency after irradiation for 5 h. After loading Pt on TiO<sub>2</sub>, however, the photocatalytic H<sub>2</sub> evolution rate could be enhanced, and the average rate of H<sub>2</sub> evolution was up to 216.8 μmol h<sup>-1</sup> g<sup>-1</sup>. It was because Pt nanoparticles could act as active sites to store electrons and the recombination of the photoinduced electron-hole pairs could be suppressed. And the role of Pt also could be confirmed by the comparison between the PTG-x and TG-x samples (Fig. S8). After the introduction of rGO, an immense enhancement of H<sub>2</sub> generation was demonstrated. And the amount of evolved H<sub>2</sub> increased with increasing rGO content up to 2 wt%. The highest H<sub>2</sub> evolution rate obtained for PTG-2, was 1075.68 μmol h<sup>-1</sup> g<sup>-1</sup>, which was 81 times and 5 times higher than that of the pure TiO<sub>2</sub> and PT samples, respectively. Compared to PT sample, the enhanced specific surface area of PTG composites as witnessed from the BET analysis in Fig. 3 and Table S1 had increased the reaction sites availability thus facilitating reactants adsorption[57]. Furthermore, rGO could effectively enhance migration of the photogenerated charges thereby promoting faster accessibility to the reaction sites and enhancing the initiation of the photocatalytic reaction. The extended light absorption into the visible light region (Fig. 4) had also contributed to the improved photocatalytic capability of PTG composites. On the contrary, despite the enhanced BET specific surface area, visible light absorption and photogenerated charges transportation, the rate of H<sub>2</sub> generation removal showed a decreasing trend in PTG-3 and PTG-5, which could be related to the excessive rGO increased the opportunity for the collision of electrons and holes and

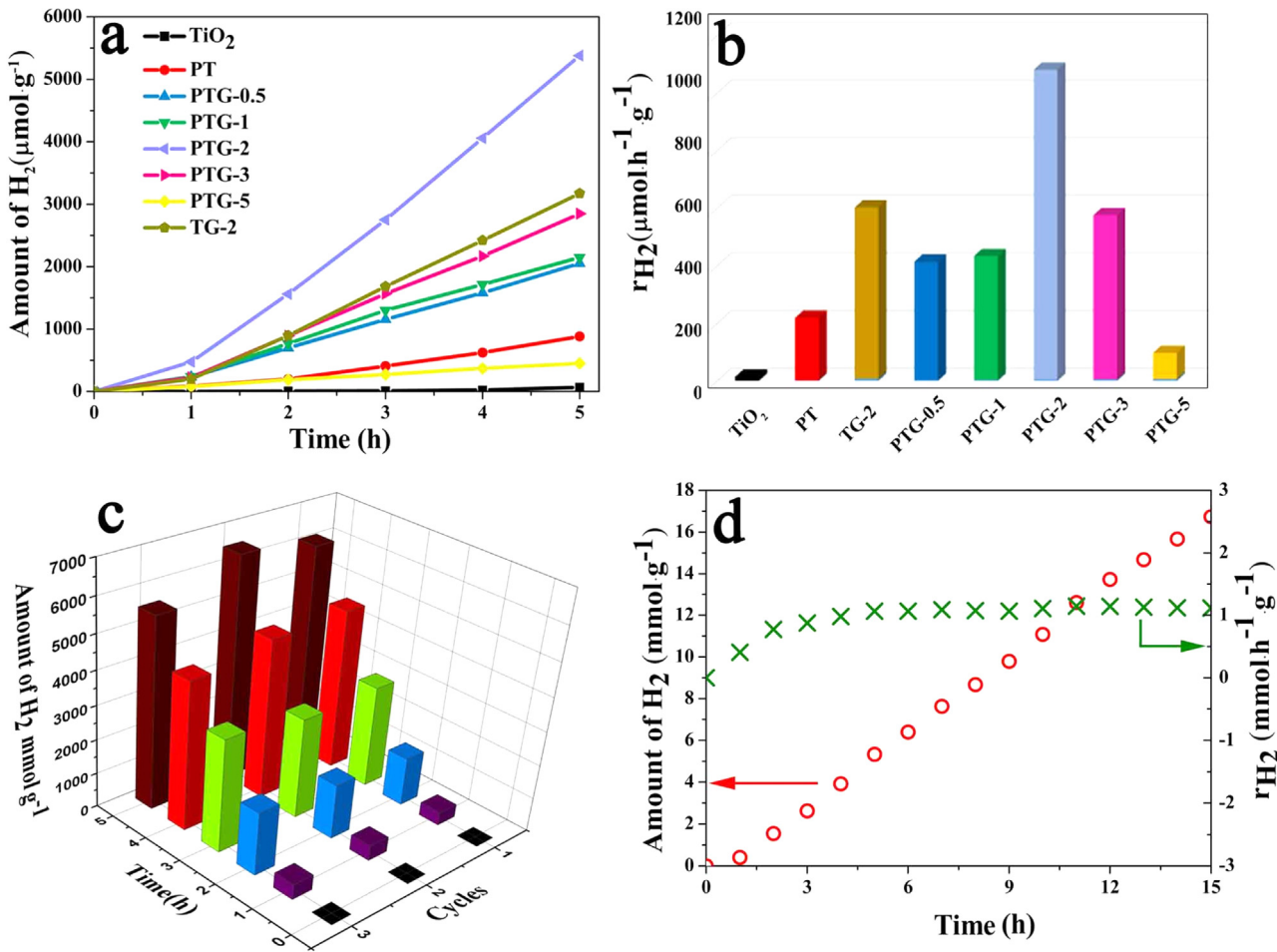


**Fig. 6.** (a) H<sub>2</sub> generation profile and (b) rate ( $r_{\text{H}_2}$ ) of hydrogen generation for different samples. (c) the stability study and (d) hydrogen generation from a continuous measurement for PTG-2.

promoted the recombination of the photo-induced charges [58]. On the other hand, the excessive rGO increased in the opacity and light scattering, which could lead to shielding the active sites of the photocatalysts [27,40].

Due to the outstanding photocatalytic of PTG-2, the photostability was further studied. As shown in Fig. 6c and d, the photostability of PTG-2 was investigated by performing the recycle experiments and the continuous irradiation for 15 h. After three recycles or continuous irradiation for 15 h, the amount of H<sub>2</sub> and the H<sub>2</sub> evolution rate had no obvious degradation. So it was suggested that the present PTG-2 nanocomposite was easily recovered and re-used for photocatalytic H<sub>2</sub> generation under the same condition. It was known that one of the crucial factors in determining the viability of using the photocatalysts for hydrogen generation was the prospect of recovery and reusability. And if the photocatalysts were unrecoverable, they may result in a secondary pollution of the effluent water after a treatment process, which would become a potential threat to human health and the ecosystem.

According to the ESR results, PTG-2 could also serve as a catalyst to degrade organic dyes. So we carried out the photocatalytic degradation of methylene orange (MO) in aqueous solution (10 mg L<sup>-1</sup>) in the presence of 300W Xe lamp and solar simulator, respectively. The photocatalytic activity of TiO<sub>2</sub>, PT, PTG-2 and TG-2 were monitored by measuring maximum absorbance of MO at 465 nm (Fig. S9-12). As can be seen from Fig. S9-12, PTG-2 had the highest removal rate in the presence of either solar simulator or 300W Xe lamp. Interestingly, up to 94% MO was decomposed in 10 min in the presence of 300W Xe lamp. And after repeating the photocatalytic

degradation of MO three times, the PTG-2 sample in the reaction still displayed a similar photocatalytic efficiency (Fig. S13). Furthermore, the kinetics for MO degradation were also investigated. The plots of  $-\ln([A_t]/[A_0])$  and  $1/[A_t] - 1/[A_0]$  versus time were shown in Fig. S14, and they displayed straight line, suggesting the MO degradation obeyed a second-order process. And the highest MO degradation performance was ascribed to the exist of rGO, the photogenerated electrons transferred to rGO sheet which reduced the probability of electron-hole recombination and enhanced the separation efficiency. And the excited holes in the VB of TiO<sub>2</sub> helped produce hydroxyl radicals ( $\cdot\text{OH}$ ) along with other oxidants, such as O<sub>2</sub><sup>-</sup>, H<sub>2</sub>O<sub>2</sub>, to decompose MO.

### 3.3. Mechanism of the enhanced photocatalytic hydrogen generation

To understand the mutual interaction and electronic structures of the rGO/TiO<sub>2</sub> nanocomposite structure, density functional theory (DFT) calculations were carried out. We constructed a cluster model which consisted of spherical anatase TiO<sub>2</sub> cluster and graphene nanosheet (Fig. 7a and b). Our calculated results revealed the adhesion energy was a negative value (-0.481 eV) corresponding to a stabilizing interaction between the TiO<sub>2</sub> cluster and graphene substrate. For TiO<sub>2</sub> cluster, the valence band edge is primarily derived from O2p orbitals while the conduct band edge from Ti4d orbitals, and resulted in a bandgap of 2.92 eV (Fig. 7c), which was smaller than its bulk value (3.16 eV) caused by the nano-size effect of the constructed cluster. However, its relative values could still illustrate

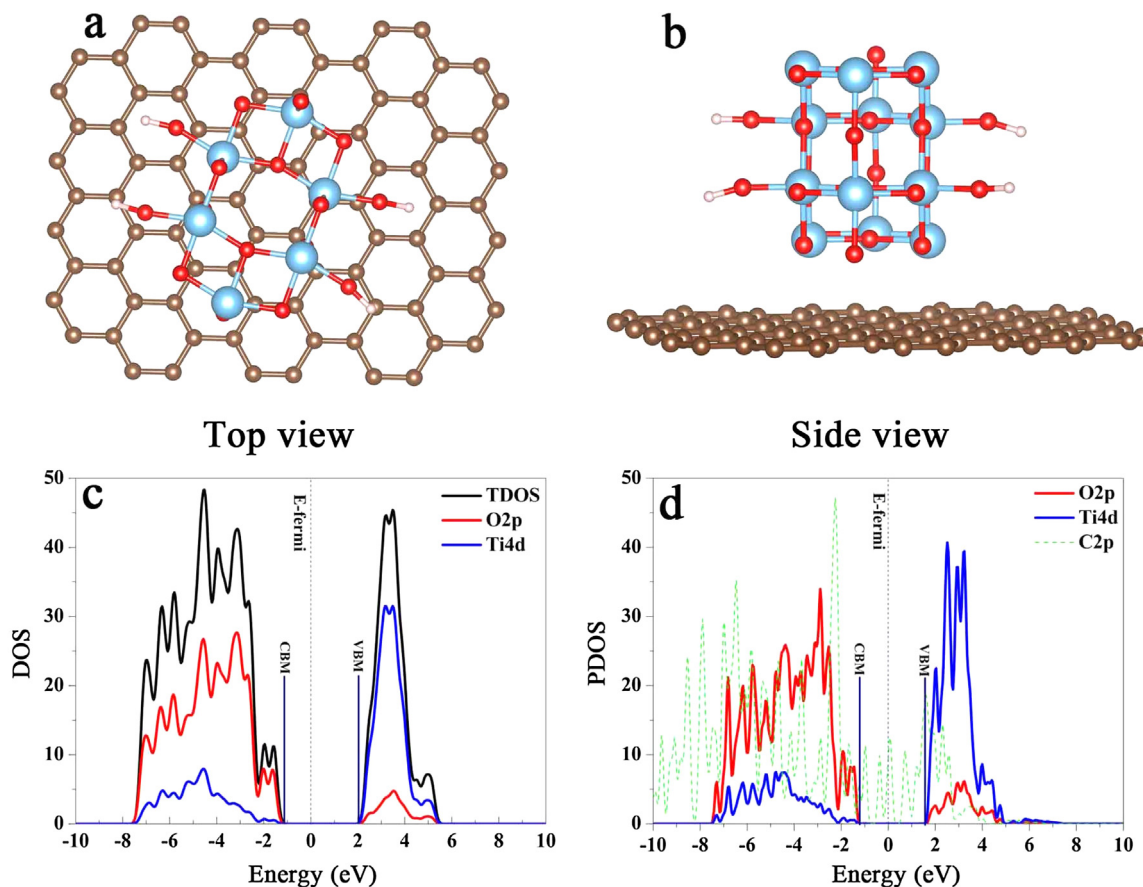


**Fig. 7.** Energy band structures of anatase  $\text{TiO}_2$  and graphene/ $\text{TiO}_2$  composites. Constructed cluster model from top (a) and side (b) view, (c) DOS of  $\text{TiO}_2$  (d) PDOS of graphene/ $\text{TiO}_2$  composites.

the electronic changes after compositing with graphene. Compared with  $\text{TiO}_2$  cluster, a prominent change was the downshift of the conduction band edge in nanocomposite with a bandgap of 2.76 eV (Fig. 7d), which was in good agreement with the observed results by UV-vis absorption spectra. Besides, the original blank energy region located at  $\text{TiO}_2$  bandgap was filled with  $\text{C}2\text{p}$  orbitals as plotted by the green dash line and functionalized as impurity state, which resulted in excited electrons after illuminating in  $\text{TiO}_2$  transferring to graphene.

To further prove and understand the photocatalytic mechanism, the PEC performances of  $\text{TiO}_2$ , PT, TG and PTG-2 samples were investigated by measuring the photocurrent densities. We first measured the photocurrent response in a three-electrode electrochemical cell with Ag/AgCl as the reference electrode and Pt foil as the counter electrode. As can be seen from Fig. 8a, PTG-2 sample exhibited the lowest photocurrent onset potential. And under irradiation, obvious current responses could be discerned from  $-0.15$  to  $1.15$  eV (vs RHE). PTG-2 showed the highest photocurrent density, followed by TG, PT, and then pure  $\text{TiO}_2$ , indicating that PTG-2 should be better semiconductor material for solar light harvesting. Therefore, PTG-2 nanocomposite had the highest total photoconversion efficiency. Furthermore, the same phenomenon could be seen from the transient photocurrent response curves (Fig. 8b). The transient photocurrent response curves of the samples were monitored by five on-off cycles of intermittent irradiation. As can be seen, there was a fast and uniform photocurrent responding with the irradiation of light turned on and off in both electrodes, indicating that the nanocomposite could act as a high-quality photosensitive catalyst [59]. And the photocurrents came from photo-generated electrons, which were excited from the valence band to conduction

band of  $\text{TiO}_2$ . The photocurrent density of  $\text{TiO}_2$  was  $0.4 \mu\text{A cm}^{-2}$ , while the photocurrent density of PTG-2 nanocomposite showed about 3 times as high as that of  $\text{TiO}_2$ . This was ascribed to the easily recombination of electron-hole pairs on  $\text{TiO}_2$ . For PTG-2, however, the photoinduced electrons were transferred effectively from  $\text{TiO}_2$  to rGO, and this significantly reduced the recombination of electron-hole pairs [60]: holes were trapped by reduced species in the electrolyte on the surface of  $\text{TiO}_2$ , while the electrons were transferred via rGO. And this also indicated that rGO was an efficient transport channel for photo-generated electrons.

Additionally, electrochemical impedance measurements were carried out in the frequency range of 1 kHz to  $0.04642$  Hz at a potential of 0 V vs Ag/AgCl under dark conditions, to investigate the electronic properties of  $\text{TiO}_2$ , PT, TG and PTG-2 samples. The electrochemical impedance spectra (EIS) of different samples were shown in Fig. 8c. EIS was an excellent method to evaluate the electron-hole pairs transport and recombination properties within the photocatalytic nanocomposites, which could be presented in the form of Nyquist plots [19]. The smaller diameter of the semi-circle in Nyquist plots indicates a lower resistance of the interfacial charge transfer across the electrode/electrolyte interface [61]. As shown in Fig. 8c, the PTG-2 composite exhibited the smallest arc diameter among the samples, indicating that the introduction of rGO could decrease the interfacial charge transfer resistance, which was ascribed to faster charge transfer and lower rate of charge recombination. And this result was in accordance with the result of transient photocurrent response, which was shown in Fig. 8a, b and Fig. S17.

We further calculated the CB position of  $\text{TiO}_2$  and PTG-2 nanocomposite from the Mott-Schottky plot (Fig. 8d).

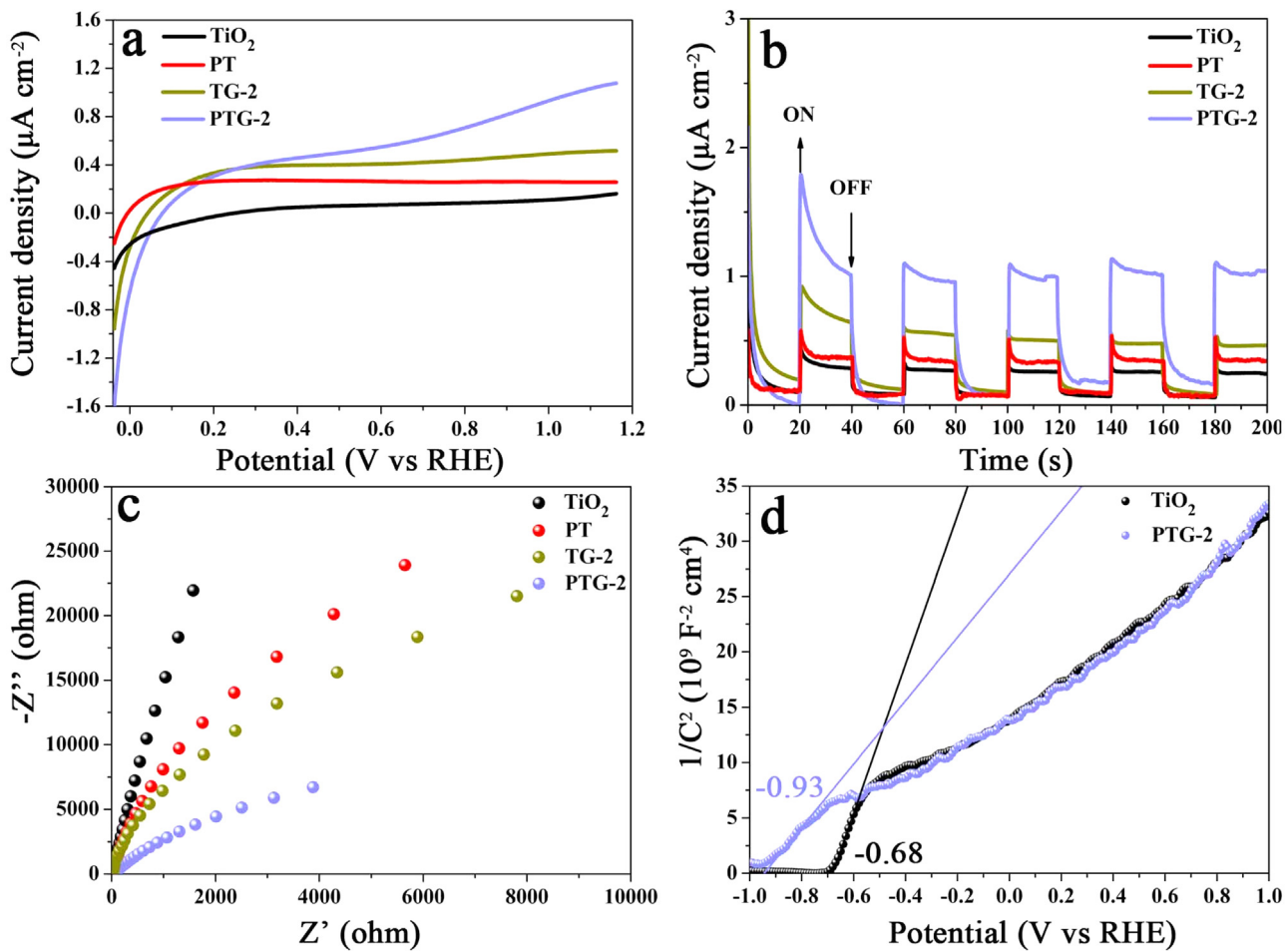


**Fig. 8.** PEC performances and characterizations of different samples: (a) J-V curves. (b) Transient photocurrent response curves. (c) Electrochemical impedance spectra. (d) Mott-Schottky plots.

Mott-Schottky measurement was an excellent method to determine the conduction type, CB position and carrier concentrations of photocatalyst. As shown in Fig. 8d, the  $\text{TiO}_2$  and PTG-2 samples both showed a positive slope in the Mott-Schottky plots, indicating that the samples were n-type semiconductors with electron conduction. According to the Mott-Schottky plot, the value of flat band potential ( $E_{fb}$ ) could be obtained from the x-intercept of the linear region of the curve  $1/C^2$  vs  $V$  [62]. The observed  $E_{fb}$  (CB) for  $\text{TiO}_2$  and PTG-2 were  $-0.68 \text{ V}$  and  $-0.93 \text{ V}$ , respectively. So, the bottom level of the conduction band of PTG-2 nanocomposite was much more negative than the reduction potential of  $\text{H}^+/\text{H}_2$  ( $0 \text{ V}$ ), and according to the photocatalytic theory, PTG-2 had a stronger reduction ability to reduce water to  $\text{H}_2$  upon excitation than  $\text{TiO}_2$  [63]. In addition, the donor concentration of the n-type PTG-2 semiconductor could be quantified by the Mott-Schottky equation:

$$\frac{1}{C^2} = \frac{2}{e\epsilon_0\epsilon N_d} [(V - V_{fb}) - kT/e] \quad (1)$$

where  $C$  was the capacitance of the space charge region,  $e$  was the electron charge of  $1.602 \times 10^{-19} \text{ C}$ ,  $\epsilon$  was the relative permittivity of 48 [11],  $\epsilon_0$  was the vacuum permittivity of  $8.854 \times 10^{12} \text{ F m}^{-1}$ ,  $V$  was the electrode applied potential,  $k$  was the Boltzmann constant,  $T$  was the absolute temperature, and  $N_d$  was the carrier density. However, the term of  $kT/e$  was exceedingly small at room temperature, so it was neglected. Then, Eq. (5) could be simplified to

$$N_d = \frac{2}{e\epsilon_0\epsilon} / \frac{d(1/C^2)}{dV} \quad (2)$$

and the calculated carrier density of PTG-2 was  $1.02 \times 10^{20} \text{ cm}^{-3}$ , while the carrier density of  $\text{TiO}_2$  was  $4.38 \times 10^{19} \text{ cm}^{-3}$  [62]. The electron density of PTG-2 was about 1 orders magnitude higher than that of  $\text{TiO}_2$ , indicating PTG-2 had a much faster carrier transfer, and this could be beneficial to the performance of photocatalytic hydrogen production. According to the results of  $E_g$  and CB, the VB could be determined to  $+1.83 \text{ eV}$ . And combining the above results, a schematic illustration of the band position in the potential vs NHE energy diagram for PTG-2 was shown in Fig. 9(a). As it could be seen, the electronic structures of the pristine  $\text{TiO}_2$  had been modified successfully, which was attributed to the  $\text{Ti}-\text{O}-\text{C}$  bonds between  $\text{TiO}_2$  and rGO (Figs. 2 and 3).

Depending on the above analysis, the outstanding photocatalytic performance of PTG-2 could be understood as shown in Fig. 9b. The schematic illustrated the mechanism of charge transfer from  $\text{TiO}_2$  to rGO via the interfaces supported by  $\text{Ti}-\text{O}-\text{C}$  bonds, which gave a path for the electrons transfer from  $\text{TiO}_2$  to rGO and hindered the recombination of electron-hole pairs. It is widely known that photocatalytic reactions include four major steps: (1) photocatalysts absorb solar light; (2) electron-hole pairs are produced by photoexcitation; (3) electron-hole pairs separation and migration to the surface of photocatalysts; (4) redox reaction on the surface [64]. The activity of photocatalytic reactions is associated with the characteristics of photocatalysts, these include electronic, crystal, surface and structure. And an integrated engineering of the above actors could efficiently accelerate the performance of photocatalytic hydrogen generation. Firstly, the narrowed band gap of

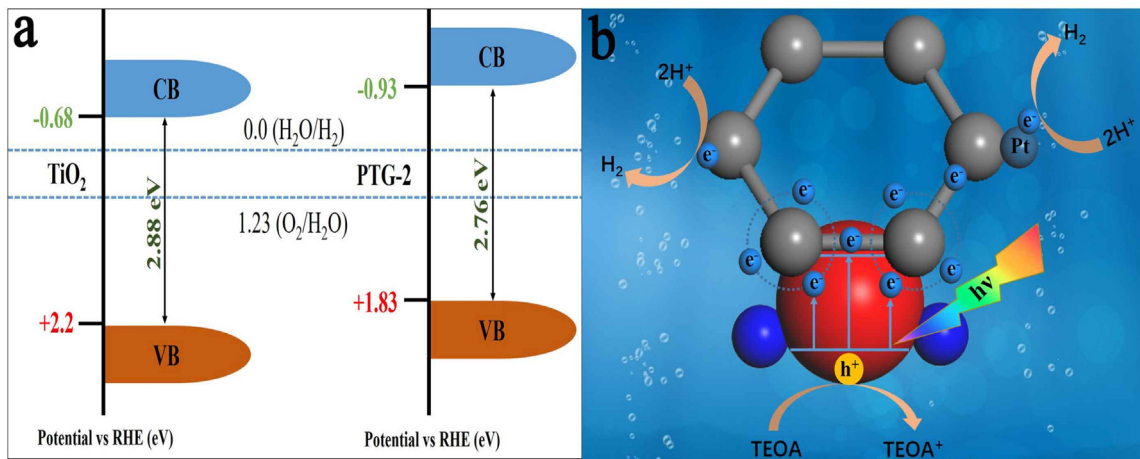


**Fig. 9.** (a) Calculated bandgap diagrams. (b) Proposed mechanism for photocatalytic H<sub>2</sub> generation on PTG.

PTG-2 could accelerate light absorption, and with the improved light absorption property (Fig. 4(a)), the PTG-2 nanocomposite could absorb more light include visible light. And under full solar light irradiation, electrons (e<sup>-</sup>) were excited from the conduction band (CB) and creating holes (h<sup>+</sup>) in the VB. Secondly, part of these electrons would access to C2p orbitals of graphene, and the others would be excited to the conduction band (CB) of TiO<sub>2</sub>. Then, these electrons would be attracted immediately to rGO due to the electrostatic force and rapidly transformed them to Pt nanoparticles, where the rGO acted as a “superhighway” for the transport of electrons [11], leading to hole-electron separation. This was ascribed to the two-dimensional  $\pi$ -conjugation structure of rGO, and it was a high work function material with excellent electron-accepting and transport properties. Furthermore, the recombination of charge pairs could be diminished by the large specific surface area [65]. Finally, the electrons could effectively reduce H<sub>2</sub>O to produce H<sub>2</sub>, while holes reacted with TEOA as a sacrificial reagent. The major routes in the photocatalytic H<sub>2</sub> production mechanism under full solar light irradiation were described as: Eqs. (3)–(7).



#### 4. Conclusions

In summary, the present work demonstrated the strong synergistic interaction between rGO and semiconductor, which improved the light adsorption and charge separation properties. FT-IR and XPS analysis confirmed the formation of Ti—O—C bonds in the PTG composites, resulting in the emergence of new optical band edge. The DFT calculations of the interaction between the building unit TiO<sub>2</sub> and graphene show that this interaction was strong and the band gap was narrowed efficiently. The photocatalytic hydrogen evolution ability from TEOA-water solution could be remarkably enhanced by the PTG composite with the rGO content of 2 wt%, and the maximum photocatalytic hydrogen generation rate was 1075.68  $\mu\text{mol h}^{-1} \text{g}^{-1}$  under the full solar wavelength range of light. In addition, the photocatalysts showed excellent photostability, which was an important ability for practical application. This outstanding activity and stability of the Pt/TiO<sub>2</sub>/rGO composite could be attributed to the synergistic effect among Pt, TiO<sub>2</sub> and

rGO, which could promote the transitive property of electrons so as to extremely inhibit the recombination of photoinduced electron-hole pairs. This study showed a clear photocatalysis mechanism of Pt/TiO<sub>2</sub>/rGO composite and opened up new insights to improve the photocatalytic activity of semiconductors.

#### Acknowledgment

The authors gratefully acknowledge the financial support provided by the National Nature Science Foundation of China as general projects (21377061, National Science and Technology Major Project (Grant No. 2016ZX05058-003-004), and by Natural Science Foundation of Tianjin (Grant No. 15JCYBJC48400, 15JCZDJC41200 and 16YFZCSF00300).

#### Appendix A. Supplementary data

Supplementary data associated with this article can be found, in the online version, at <http://dx.doi.org/10.1016/j.apcatb.2017.02.031>.

#### References

- [1] Z.L. Wu, C.H. Wang, B. Zhao, J. Dong, F. Lu, W.H. Wang, W.C. Wang, G.J. Wu, J.Z. Cui, P. Cheng, *Angew. Chem. Int. Ed.* 55 (2016) 4938–4942.
- [2] C. Li, C. Koenigsmann, W. Ding, B. Rudshteyn, K.R. Yang, K.P. Regan, S.J. Konezny, V.S. Batista, G.W. Brudvig, C.A. Schmuttenmaer, J.H. Kim, *J. Am. Chem. Soc.* 137 (2015) 1520–1529.
- [3] K. Maeda, K. Domen, *J. Phys. Chem. Lett.* 1 (2010) 2655–2661.
- [4] Z. Jiang, Y. Liu, T. Jing, B. Huang, Z. Wang, X. Zhang, X. Qin, Y. Dai, *Appl. Catal. B: Environ.* 200 (2016) 230–236.
- [5] R. Asahi, T. Morikawa, T. Ohwaki, K. Aoki, Y. Taga, *Science* 293 (2001) 269–271.
- [6] S.U.M. Khan, M. Al-Shahry, W.B. Ingler Jr., *Science* 297 (2002) 2243–2245.
- [7] A. Sinhamahapatra, J.P. Jeon, J.S. Yu, *Energy Environ. Sci.* 8 (2015) 3539–3544.
- [8] X. Chen, S. Shen, L. Guo, S.S. Mao, *Chem. Rev.* 110 (2010) 6503–6570.
- [9] G. Liu, L.C. Yin, J. Wang, P. Niu, C. Zhen, Y. Xie, H.M. Cheng, *Energy Environ. Sci.* 5 (2012) 9603–9610.
- [10] W.J. Yin, H. Tang, S.H. Wei, M.M. Al-Jassim, J. Turner, Y. Yan, *Phys. Rev. B* 82 (2010) 045106.
- [11] C. Zhao, H. Luo, F. Chen, P. Zhang, L. Yi, K. You, *Energy Environ. Sci.* 7 (2014) 1700–1707.
- [12] D.P. Colombo Jr., K.A. Roussel, J. Saeh, D.E. Skinner, J.J. Cavalieri, R.M. Bowman, *Chem. Phys. Lett.* 232 (1995) 207–214.
- [13] A. Testino, I.R. Bellobono, V. Buscaglia, C. Canevali, M. D'Arienzo, S. Polizzi, R. Scotti, F. Morazzoni, *J. Am. Chem. Soc.* 129 (2007) 3564–3575.
- [14] M. Kong, Y. Li, X. Chen, T. Tian, P. Fang, F. Zheng, X. Zhao, *J. Am. Chem. Soc.* 133 (2011) 16414–16417.
- [15] M. Reza Gholipour, C.-T. Dinh, F. Béland, T.O. Do, *Nanoscale* 7 (2015) 8187–8208.
- [16] M. Murdoch, G.I.N. Waterhouse, M.A. Nadeem, J.B. Metson, M.A. Keane, R.F. Howe, J. Llorca, H. Idriss, *Nat. Chem.* 3 (2011) 489–492.
- [17] H. Park, H.i. Kim, G.h. Moon, W. Choi, *Energy Environ. Sci.* 9 (2016) 411–433.

- [18] Y. Sang, Z. Zhao, J. Tian, P. Hao, H. Jiang, H. Liu, J.P. Claverie, *Small* 10 (2014) 3775–3782.
- [19] G. Xie, K. Zhang, B. Guo, Q. Liu, L. Fang, J.R. Gong, *Adv. Mater.* 25 (2013) 3820–3839.
- [20] S. Morales Torres, L.M. Pastrana Martínez, J.L. Figueiredo, J.L. Faria, A.M.T. Silva, *Environ. Sci. Pollut. Res.* 19 (2012) 3676–3687.
- [21] X. Wang, A.L. Zhi, K. Müllen, *Transparent Nano Lett.* 8 (2008) 323–327.
- [22] W. Chen, L. Yan, P.R. Bangal, *Carbon* 48 (2010) 1146–1152.
- [23] S.G. Park, B. Magyari-Köpe, Y. Nishi, *Phys. Rev. B* 82 (2010) 115109.
- [24] G. Kresse, J. Hafner, *Phys. Rev. B* 47 (1993) 558.
- [25] G. Kresse, J. Furthmüller, *Comp. Mater. Sci.* 6 (1996) 15–50.
- [26] D.M. Ceperley, B.J. Alder, *Phys. Rev. Lett.* 45 (1980) 566.
- [27] P. Cheng, Z. Yang, H. Wang, W. Cheng, M. Chen, W. Shangguan, G. Ding, *Int. J. Hydrogen Energy* 37 (2012) 2224–2230.
- [28] G. Chen, M. Sun, Q. Wei, Y. Zhang, B. Zhu, B. Du, J. Hazard. Mater. 244–245 (2013) 86–93.
- [29] W. Gao, M. Wang, C. Ran, X. Yao, H. Yang, J. Liu, D. He, J. Bai, *Nanoscale* 6 (2014) 5498–5508.
- [30] J.M. Liu, Q.C. Zhang, J.C. Yang, *Chem. Commun.* 50 (2014) 13971–13974.
- [31] X. Li, W. Bi, L. Zhang, S. Tao, W. Chu, Q. Zhang, Y. Luo, C. Wu, Y. Xie, *Adv. Mater.* 28 (2016) 2427–2431.
- [32] L. Nguyen, S. Zhang, L. Wang, Y. Li, H. Yoshida, A. Patlolla, S. Takeda, A.I. Frenkel, F. Tao, *ACS Catal.* 6 (2016) 840–850.
- [33] B. Chai, T. Peng, J. Mao, K. Li, L. Zan, *Phys. Chem. Chem. Phys.* 14 (2012) 16745–16752.
- [34] G. Jiang, Z. Lin, C. Chen, L. Zhu, Q. Chang, N. Wang, W. Wei, H. Tang, *Carbon* 49 (2011) 2693–2701.
- [35] H. Yu, Y. Zhao, C. Zhou, L. Shang, Y. Peng, Y. Cao, L.Z. Wu, C.H. Tung, T. Zhang, *J. Mater. Chem. A* 2 (2014) 3344–3351.
- [36] Q. Xiang, J. Yu, M. Jaroniec, *J. Am. Chem. Soc.* 134 (2012) 6575–6578.
- [37] H.N. Kim, H. Yoo, J.H. Moon, *Nanoscale* 5 (2013) 4200–4204.
- [38] J.S. Jang, S.H. Choi, H.G. Kim, J.S. Lee, *J. Phys. Chem. C* 112 (2008) 17200–17205.
- [39] B. Chai, T. Peng, P. Zeng, J. Mao, *J. Mater. Chem.* 21 (2011) 14587–14593.
- [40] Q. Xiang, J. Yu, M. Jaroniec, *J. Phys. Chem. C* 115 (2011) 7355–7363.
- [41] G. Li, T. Wang, Y. Zhu, S. Zhang, C. Mao, J. Wu, B. Jin, Y. Tian, *Appl. Surf. Sci.* 257 (2011) 6568–6572.
- [42] L. Karimi, M.E. Yazdanshenas, R. Khajavi, A. Rashidi, M. Mirjalili, *Cellulose* 21 (2014) 3813–3827.
- [43] J. Liu, H. Bai, Y. Wang, Z. Liu, X. Zhang, D.D. Sun, *Adv. Funct. Mater.* 20 (2010) 4175–4181.
- [44] G. Williams, B. Seger, P.V. Kamat, *ACS Nano* 2 (2008) 1487–1491.
- [45] V. Lee, L. Whittaker, C. Jaye, K.M. Baroudi, D.A. Fischer, S. Banerjee, *Chem. Mater.* 21 (2009) 3905–3916.
- [46] X. Pan, Y. Zhao, S. Liu, C.L. Korzeniewski, S. Wang, Z. Fan, *ACS Appl. Mater. Interfaces* 4 (2012) 3944–3950.
- [47] T.M.G. Mohiuddin, A. Lombardo, R.R. Nair, A. Bonetti, G. Savini, R. Jalil, *Phys. Rev. B* 79 (2009) 1–9.
- [48] Z.A. Lan, G. Zhang, X. Wang, *Appl. Catal. B: Environ.* 192 (2016) 116–125.
- [49] H. Zhang, X. Lv, Y. Li, Y. Wang, J. Li, *ACS Nano* 4 (2010) 380–386.
- [50] G. Fu, S.T. Sanjay, X. Li, *Analyst* 141 (2016) 3883–3889.
- [51] J. Liu, Y. Liu, N. Liu, Y. Han, X. Zhang, H. Huang, Y. Lifshitz, S.-T. Lee, J. Zhong, Z. Kang, *Science* 347 (2015) 970–974.
- [52] F. Hao, C.C. Stoumpos, R.P.H. Chang, M.G. Kanatzidis, *J. Am. Chem. Soc.* 136 (2014) 8094–8099.
- [53] S. Liang, Y. Xia, S. Zhu, S. Zheng, Y. He, J. Bi, M. Liu, L. Wu, *Appl. Surf. Sci.* 358 (2015) 304–312.
- [54] X. Gong, M. Tong, F.G. Brunetti, J. Seo, Y. Sun, D. Moses, F. Wudl, A.J. Heeger, *Adv. Mater.* 23 (2011) 2272–2277.
- [55] A. Kudo, Y. Miseki, *Chem. Soc. Rev.* 38 (2009) 253–278.
- [56] X. Bai, L. Wang, R. Zong, Y. Zhu, *J. Phys. Chem. C* 117 (2013) 9952–9961.
- [57] S.S. Lee, H. Bai, Z. Liu, D.D. Sun, *Appl. Catal. B: Environ.* 140–141 (2013) 68–81.
- [58] X.Y. Zhang, H.P. Li, X.L. Cui, Y. Lin, *J. Mater. Chem.* 20 (2010) 2801–2806.
- [59] Y. Tian, L. Wang, H. Tang, W. Zhou, *J. Mater. Chem. A* 3 (2015) 11294–11301.
- [60] J. Yu, G. Dai, B. Cheng, *J. Phys. Chem. C* 114 (2010) 19378–19385.
- [61] L. Yu, L. Xiong, Y. Yu, *J. Phys. Chem. C* 119 (2015) 22803–22811.
- [62] G. Wang, Q. Wang, W. Lu, J. Li, *J. Phys. Chem. B* 110 (2006) 22029–22034.
- [63] G.S. Zeng, J. Yu, H.Y. Zhu, H.L. Liu, Q.J. Xing, S.K. Bao, S. He, J.P. Zou, C.T. Au, *RSC Adv.* 5 (2015) 37603–37609.
- [64] J. Ran, T.Y. Ma, G. Gao, X.W. Du, S.Z. Qiao, *Energy Environ. Sci.* 8 (2015) 3708–3717.
- [65] Y.F. Li, Z.P. Liu, *J. Am. Chem. Soc.* 133 (2011) 15743–15752.